


 Cite this: *New J. Chem.*, 2021, 45, 11304

Light-emitting analogues based on triphenylamine modified quinoxaline and pyridine[2,3-*b*]pyrazine exhibiting different mechanochromic luminescence†

 Yuxi Ge^a and Bin Huang *^{ab}

A series of light-emitting analogues, [4-(2,3-diphenyl-quinoxalin-6-yl)-phenyl]-diphenyl-amine (**TPA-DPQ**) and [4-(2,3-diphenyl-pyrido[2,3-*b*]pyrazin-7-yl)-phenyl]-diphenyl-amine (**TPA-DPP**) are synthesized and characterized. **TPA-DPQ** and **TPA-DPP** possess similar donor–acceptor structures, in which triphenylamine is used as an electron donor while 2,3-diphenyl-quinoxaline (DPQ) and its analogue 2,3-diphenyl-pyridine[2,3-*b*]pyrazine (DPP) serve as electron acceptors. Due to the stronger electron-withdrawing ability of DPP compared with DPQ, **TPA-DPP** exhibits longer but weaker emission than **TPA-DPQ** as expected. However, **TPA-DPQ** and **TPA-DPP** show different mechanochromic luminescence (MCL) properties with emission color changes of 42 and 10 nm, respectively. Crystallographic analysis demonstrates that changes of CH... π and CH...N intermolecular interactions are responsible for the significantly different MCL behaviors of the two compounds. This work will provide some guidance for the rational design of MCL-active fluorophores.

 Received 22nd March 2021,
 Accepted 19th May 2021

DOI: 10.1039/d1nj01350e

rsc.li/njc

1. Introduction

Mechanochromic luminescent (MCL) emitters are smart fluorophores that show a reversible change in photoluminescence (PL) color upon external stimuli such as mechanical stress (*e.g.* grinding, pressing, crushing, scratching, and shearing), heat treatment, and solvent vapor fuming.^{1–4} Recently, MCL materials have become materials of interest for their potential applications in solid-state sensors, optoelectronic devices, optical storage and security inks.^{5–8} Most reports show that the change of molecular conformations, packing and intermolecular interactions under an external stimuli are considered to be key factors for MCL properties.^{9,10} Therefore, the development of novel MCL emitters with well-defined crystal structures is indispensable for the elaboration of the MCL mechanism.

Compared with conventional fluorophores, due to the lack of a clear design strategy, MCL fluorophores remain limited in number. Considerable efforts were devoted to enrich the library

of MCL emitters. For example, tetraphenylethene (TPE) is a well-known building block, which has been successfully introduced to construct most MCL emitters.^{11–15} Other luminogens such as the β -diketone boron complex,¹⁶ pyrene,¹⁷ phenothiazine,¹⁸ anthracene¹⁹ *etc.* can also serve as key units of some MCL materials. Besides, some donor–acceptor (D–A) type compounds have been demonstrated to be MCL fluorophores.^{20–30} The D–A structure endows enriched structural deformation and abundant intermolecular interaction variations upon external stimuli, which may result in tunable color of the solid-state emission and be responsible for MCL properties. Moreover, exploration of MCL emitters from many fluorophores featuring D–A structures may bring a new perspective for the development of novel MCL emitters.

In recent years, quinoxaline derivative compounds have attracted considerable attention because of their promising applications in some fields such as perovskite solar cells,³¹ organic light-emitting diodes³² and chemosensors.³³ Meanwhile, some quinoxaline-based fluorophores (summarized in Fig. S1, ESI†) with D–A structures show MCL properties.^{34–39} It is found that MCL properties of these compounds can be tuned by changing the electron donors while fixing the electron acceptors.^{34–38} Alternatively, modifications on the electron donors may provide another strategy for fine-tuning MCL properties of fluorophores. In this work, a quinoxaline derivative [4-(2,3-diphenyl-quinoxalin-6-yl)-phenyl]-diphenyl-amine⁴⁰ (**TPA-DPQ**, Fig. 1) is found to be MCL-active. To investigate the

^a College of Life Sciences and Chemistry, Jiangsu Key Laboratory of Biofunctional Molecule, Institute of New Materials for Vehicles, Jiangsu Second Normal University, Nanjing, 210013, P. R. China. E-mail: huangbinhb31@sina.com

^b State Key Laboratory of Bioelectronics, Jiangsu Key Laboratory for Biomaterials and Devices, School of Biological Science and Medical Engineering, Southeast University, Nanjing 210096, P. R. China

† Electronic supplementary information (ESI) available. CCDC 2065097, 2065098, 2075146 and 2080880. For ESI and crystallographic data in CIF or other electronic format see DOI: 10.1039/d1nj01350e

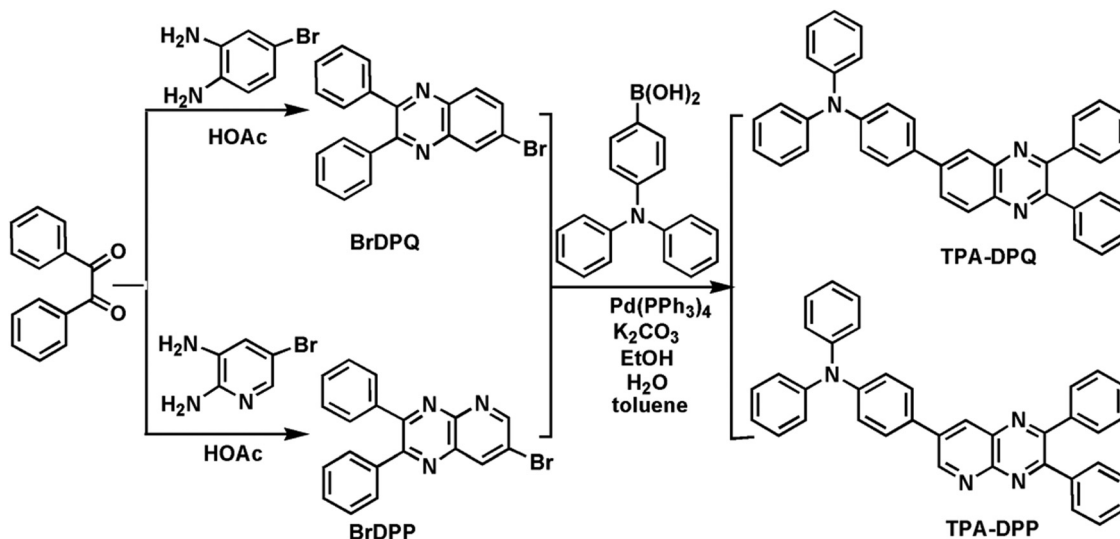


Fig. 1 Synthetic routes of TPA-DPQ and TPA-DPP.

influence of the electron acceptors on the MCL properties, we designed and synthesized an analogue of TPA-DPQ, namely [4-(2,3-diphenyl-pyrido[2,3-*b*]pyrazin-7-yl)-phenyl]-diphenyl-amine (TPA-DPP) (Fig. 1), in which triphenylamine is used as an electron donor while 2,3-diphenyl-pyridine[2,3-*b*]pyrazine (DPP) serves as an electron acceptor. TPA-DPP exhibits longer but weaker emission than TPA-DPQ, which can be attributed to the stronger electron-withdrawing ability of DPP compared to 2,3-diphenyl-quinoxaline (DPQ). However, TPA-DPQ and TPA-DPP show different MCL properties with emission color changes of 42 and 10 nm, respectively. Crystallographic analysis demonstrates that TPA-DPQ and TPA-DPP show similar highly twisted structures but minor differences in weak CH \cdots π and CH \cdots N intermolecular interactions. The totally different MCL properties of TPA-DPQ and TPA-DPP under external stimuli can be attributed to the differences in intermolecular interactions. This work will provide some guidance for the rational design of MCL-active fluorophores.

2. Experimental

2.1. General information

All reagents are purchased from commercial sources and used as received without further purification. ¹H NMR spectra of the products are recorded on a Bruker 400 NMR spectrometer with Si(CH₃)₄ as the internal standard. Mass spectra (MS) are recorded on a Thermo Electron Corporation Finnigan LTQ mass spectrometer. UV-vis absorption spectra of TPA-DPQ and TPA-DPP are obtained on a UV-vis spectrophotometer (Agilent 8453). The PL spectra, Φ_{PL} and transient PL lifetimes are investigated on an Edinburgh FLS920 spectrophotometer. Single crystal XRD measurements are carried out on a single crystal X-ray diffractometer (Oxford Gemini S Ultra) with Mo K α radiation. Differential scanning calorimetry (DSC) curves are recorded on a Netzsch DSC 2910 modulated calorimeter under a dry nitrogen atmosphere at a heating rate of 10 °C min⁻¹.

The powder XRD curves are obtained using a diffractometer (Ultima IV) with an X-ray source of Cu K α at 40 kV and 40 mA, at a scan rate of 2° (2 θ) per 1 min. CCDC 2065097 (TPA-DPQ at 150 K), 2075146 (TPA-DPQ at 296 K), 2065098 (TPA-DPP at 193 K) and 2080880 (TPA-DPP at 296 K) contain the supplementary crystallographic data for this work.⁴¹

Density functional theory (DFT) calculations of TPA-DPQ and TPA-DPP are performed using the Gaussian 09 program package.⁴² Based on the optimized molecular structures at ground state, the excitation energies of TPA-DPQ and TPA-DPP are calculated using the time-dependent density functional theory (TD-DFT) method.⁴³

2.2. Synthesis of TPA-DPQ and TPA-DPP

Synthesis of 6-bromo-2,3-diphenylquinoxaline (BrDPQ) and TPA-DPQ is carried out according to the literature.⁴⁰

Synthesis of 7-bromo-2,3-diphenylpyrido[2,3-*b*]pyrazine (BrDPP). 1,2-Diphenyl-ethane-1,2-dione (5.0 mmol) and 5-bromo-pyridine-2,3-diamine (5.0 mmol) are dissolved in 50 mL glacial acetic acid and refluxed at 110 °C for 6 h. After cooling to room temperature and adding 50 mL of water, a gray-white precipitate is filtered and dried to produce BrDPP as a gray-white powder with a yield of 94.2%. The crude BrDPP is directly used for the next reaction without purification.

Synthesis of TPA-DPP. To a mixture of BrDPP (4 mmol) and 4-(diphenylamino)phenyl boronic acid (4 mmol) in 50 mL of toluene and 20 mL of ethanol, K₂CO₃ aqueous solution (2.0 M, 4 mL) is added. After purging with N₂ for 10 min, Pd(PPh₃)₄ (0.4 mmol) is added. The resulting mixture is refluxed under N₂ for 24 h. After cooling to room temperature, the reaction mixture is poured into 50 mL water, and extracted with dichloromethane (DCM) (2 \times 50 mL). The combined organic layer is washed with saturated aqueous NaCl solution (2 \times 20 mL), and dried over anhydrous Na₂SO₄. After removing the solvent under a vacuum, the residue is purified by silica gel column chromatography with petroleum ether/DCM (v : v = 10 : 1–5 : 1) as an eluent

to afford **TPA-DPP** as an orange solid with a yield of 54.2%. ^1H NMR(400 MHz, CDCl_3) δ (ppm): 9.50 (d, $J = 4.0$ Hz, 1H), 8.67 (d, $J = 4.0$ Hz, 1H), 7.78–7.67 (m, 4H), 7.67–7.59 (m, 2H), 7.53–7.12 (m, 18H). MS (MALDI-TOF) [m/z]: calcd. for $\text{C}_{37}\text{H}_{26}\text{N}_4$, 526.62; found: 526.85.

2.3. Single crystals of **TPA-DPQ** and **TPA-DPP**

The block-shaped yellow crystals of **TPA-DPQ** are grown from DCM/hexane ($v:v = 1:1$) solution by slow evaporation at room temperature. The needle-like orange crystals of **TPA-DPP** are grown from DCM/ethanol ($v:v = 1:1$) solution by slow evaporation at room temperature.

3. Results and discussion

3.1 Synthesis

Synthetic routes of **TPA-DPQ** and **TPA-DPP** are shown in Fig. 1. First, the key intermediates BrDPQ and BrDPP are prepared by condensation reactions of the starting material 1,2-diphenylethane-1,2-dione with 4-bromo-benzene-1,2-diamine and 5-bromo-pyridine-2,3-diamine, respectively. Then BrDPQ and BrDPP are converted to target compounds **TPA-DPQ** and **TPA-DPP** via Suzuki cross-coupling reactions with 4-(diphenylamino)phenyl boronic acid. The structures of **TPA-DPQ** and **TPA-DPP** are confirmed by ^1H NMR, MS and single-crystal analysis.

3.2. Theoretical calculations

To predict the geometric and electronic structures of **TPA-DPQ** and **TPA-DPP**, DFT calculations are carried out. As shown in Fig. 2, **TPA-DPQ** and **TPA-DPP** possess twisted structures. The highest occupied molecular orbitals (HOMOs) of **TPA-DPQ** and **TPA-DPP** are mainly dispersed over the electron-donating TPA moiety and the adjacent phenyl group or pyridine ring. In contrast, the lowest unoccupied molecular orbitals (LUMO)

Table 1 Calculated triplet and singlet excitation energies (vertical transition), oscillator strength (f), and transition configurations of **TPA-DPQ** and **TPA-DPP**

Compound	State	E (eV)	F	Main configuration	p	ΔE_{ST} (eV)
TPA-DPQ	S_1	2.75	0.33	H \rightarrow L	0.70	0.43
	S_2	3.41	0.36	H \rightarrow L+1	0.69	
	T_1	2.32	0.00	H \rightarrow L	0.55	
	T_2	2.77	0.00	H-2 \rightarrow L	0.51	
TPA-DPP	S_1	2.47	0.343	H \rightarrow L	0.70	0.33
	S_2	2.94	0.216	H-2 \rightarrow L	0.68	
	T_1	1.92	0	H \rightarrow L	0.62	
	T_2	1.95	0	H-2 \rightarrow L	0.65	

are localized on the electron-withdrawing DPQ or DPP units. **TPA-DPP** has deeper HOMO and LUMO levels than **TPA-DPQ**, which can be attributed to the stronger electron-withdrawing ability of the DPP moiety compared to the DPQ unit. Accordingly, the optical bandgap (E_g) values of **TPA-DPQ** and **TPA-DPP** are estimated to be 3.10 and 2.96 eV, respectively. Based on the theoretically optimized geometries of **TPA-DPQ** and **TPA-DPP**, TD-DFT calculations are performed to estimate the energy levels of the excited-state. **TPA-DPQ** and **TPA-DPP** show S_1 values of 2.75 and 2.61 eV, and T_1 values of 2.32 and 2.28 eV (Table 1), respectively. Correspondingly, the energy splits (ΔE_{ST} s) of **TPA-DPQ** and **TPA-DPP** are calculated to be 0.43 and 0.33 eV, respectively.

3.3 Single crystallographic analysis

The single-crystal structures of **TPA-DPQ** and **TPA-DPP** are measured at 150 and 193 K, respectively. As shown in Fig. 3 and Table 2, **TPA-DPQ** and **TPA-DPP** are both monoclinic with space groups $P2_1/c$. For **TPA-DPQ**, the compound exhibits twisted molecular configuration with a D-A dihedral angle of 38.73° between the TPA moiety and the adjacent phenyl plane of the DPQ unit. The dihedral angles between the substituted phenyl rings and quinoxaline plane are 46.35 and 48.81° ,

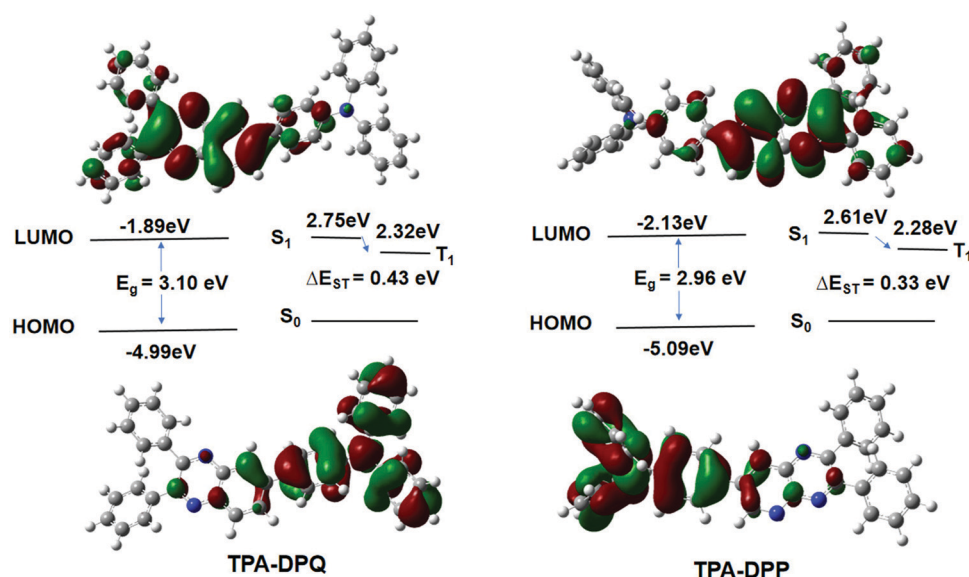


Fig. 2 Calculated energy levels for **TPA-DPQ** and **TPA-DPP**.

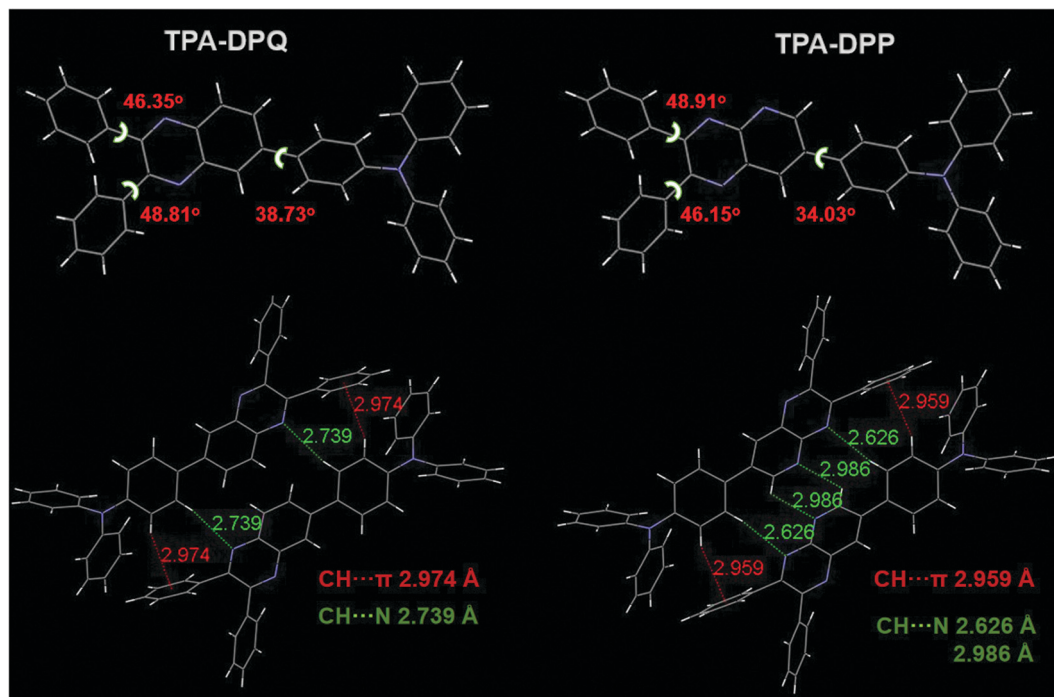


Fig. 3 The single crystal structures and molecular interactions of **TPA-DPQ** (at 150 K) and **TPA-DPP** (at 193 K).

respectively. Similar to **TPA-DPQ**, **TPA-DPP** also shows a twisted structure with a slightly smaller dihedral angle of 34.03° between the TPA moiety and the adjacent pyridine plane of the DPP unit. Similarly, the dihedral angles between the substituted phenyl rings and the pyridine[2,3-*b*]pyrazine plane are 48.91 and 46.15° , respectively.

As above mentioned, **TPA-DPQ** and **TPA-DPP** both show highly twisted structures, which may inhibit the formation of

π - π stacking arrangement in the crystals. For **TPA-DPQ**, the two neighboring molecules adopt a face-to-tail stacking mode along the *b*-axis. It is found that a phenyl ring of the TPA unit forms a close $\text{CH}\cdots\pi$ interaction with a substituted phenyl ring of the DPQ group at a distance of 2.974 Å. Meanwhile, the phenyl ring of the TPA unit also forms a $\text{CH}\cdots\text{N}$ interaction with the DPQ unit at a distance of 2.739 Å. In the case of **TPA-DPP**, the two adjacent molecules also exhibit a face-to-tail stacking

Table 2 Crystal data and structure refinement for **TPA-DPQ** and **TPA-DPP**

	TPA-DPQ	TPA-DPQ	TPA-DPP	TPA-DPP
Formula	$\text{C}_{38}\text{H}_{27}\text{N}_3$	$\text{C}_{38}\text{H}_{27}\text{N}_3$	$\text{C}_{37}\text{H}_{26}\text{N}_4$	$\text{C}_{37}\text{H}_{26}\text{N}_4$
CCDC No.	2065097	2075146	2065098	2080880
Formula weight	525.62	525.62	526.62	526.62
Space group	$P2_1/c$	$P2_1/c$	$P2_1/c$	$P2_1/c$
Temperature (K)	150	296	193	296
Wavelength/Å	0.71073	0.71073	0.71073	0.71073
Crystal system	Monoclinic	Monoclinic	Monoclinic	Monoclinic
<i>a</i> /Å	19.240(13)	19.248(18)	18.920(11)	19.065(14)
<i>b</i> /Å	8.892(6)	8.936(8)	8.897(7)	8.994(7)
<i>c</i> /Å	18.043(9)	18.090(19)	17.812(10)	17.864(14)
$\alpha/^\circ$	90.00	90.00	90.00	90.00
$\beta/^\circ$	116.87(2)	117.00(3)	116.82(2)	116.75(13)
$\gamma/^\circ$	90.00	90.00	90.00	90.00
Volume/Å ³	2754(3)	2773(5)	2676(3)	2735(4)
<i>Z</i>	4	4	4	4
Calculated density/Mg m ⁻³	1.353	1.259	1.360	1.279
<i>M</i> (mm ⁻¹)	0.074	0.074	0.078	0.076
<i>F</i> (000)	1072	1104	1104	1104
Crystal size/mm ³	0.20 × 0.15 × 0.10	0.20 × 0.15 × 0.10	0.10 × 0.10 × 0.05	0.10 × 0.08 × 0.05
No. of reflns collected	5629	6337	4743	5982
No. of unique reflns	3551	4049	2465	2892
Goodness-of-fit on <i>F</i> ²	1.027	1.022	1.043	0.970
<i>R</i> ₁ , <i>wR</i> ₂ [<i>I</i> > 2σ(<i>I</i>)]	0.0492, 0.0971	0.0528, 0.1179	0.0794, 0.1518	0.0591, 0.1393
<i>R</i> ₁ , <i>wR</i> ₂ (all data)	0.0598, 0.1305	0.0921, 0.1370	0.2049, 0.2763	0.1389, 0.1814

arrangement with $\text{CH}\cdots\pi$ interactions of 2.959 Å and $\text{CH}\cdots\text{N}$ interactions of 2.626 and 2.986 Å. Interestingly, two kinds of

$\text{CH}\cdots\text{N}$ interactions are formed, which can be attributed to the added N atom of the pyridine[2,3-*b*]pyrazine ring compared to

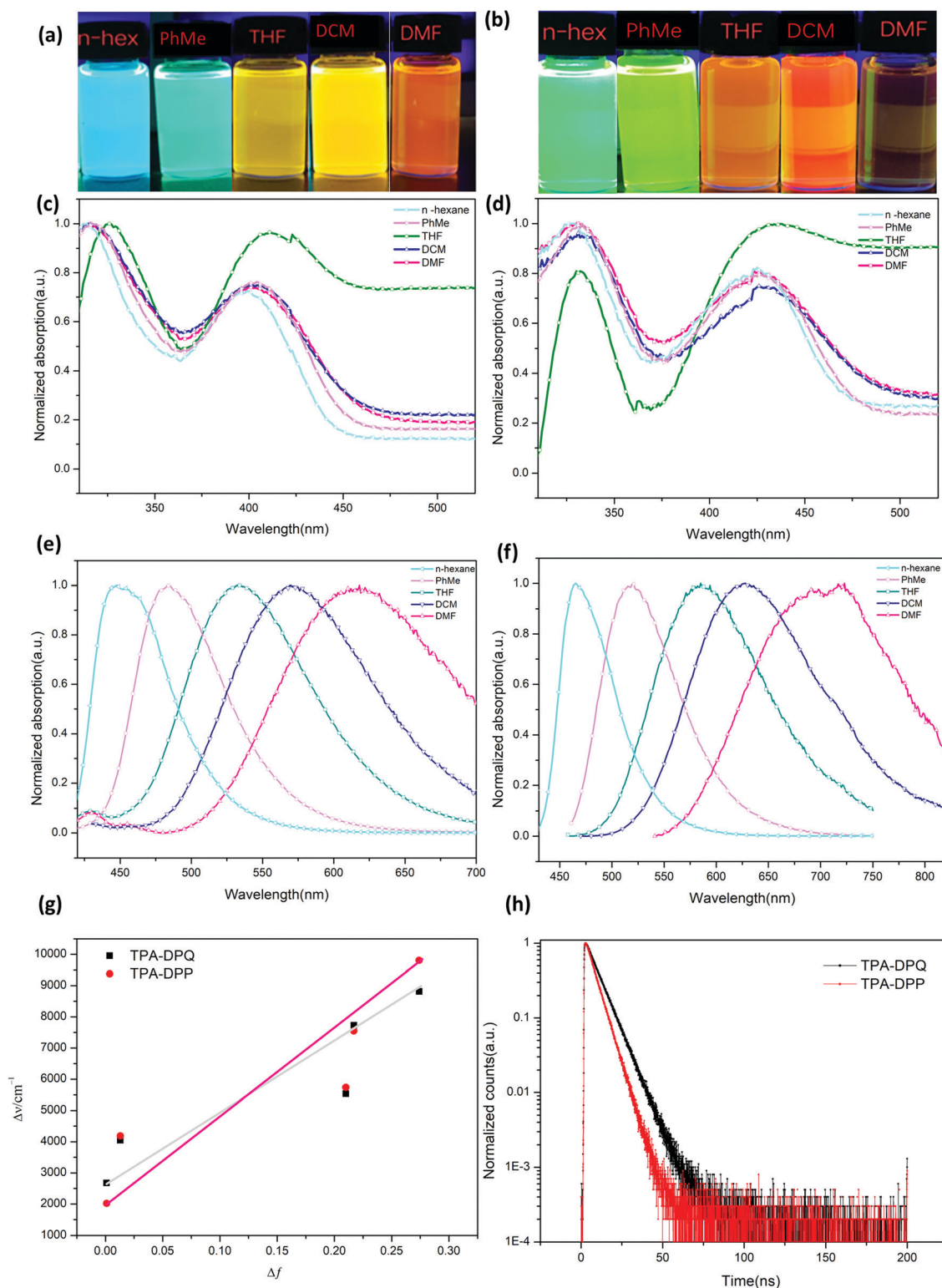


Fig. 4 (a) The digital photographs of **TPA-DPQ** in different solvents under 365 nm UV excitation; (b) the digital photographs of **TPA-DPP** in different solvents under 365 nm UV excitation; (c) UV-vis absorption spectra of **TPA-DPQ** in different solvents; (d) UV-vis absorption spectra of **TPA-DPP** in different solvents; (e) PL spectra of **TPA-DPQ** in different solvents; (f) PL spectra of **TPA-DPP** in different solvents; (g) Lippert–Mataga plots of **TPA-DPQ** and **TPA-DPP**; (h) fluorescence lifetimes of **TPA-DPQ** and **TPA-DPP** in DCM.

the quinoxaline ring. Apparently, **TPA-DPP** with shorter CH $\cdots\pi$ and CH \cdots N interactions exhibits a more compact packing than **TPA-DPQ**. It is believed that the differences in weak CH $\cdots\pi$ and CH \cdots N intermolecular interactions in crystals may have effects on the emitting behaviors of the two compounds.

To investigate the effect of temperature on molecular conformations and interactions, the single crystal structures of **TPA-DPQ** and **TPA-DPP** are also measured at 296 K (Table 2). As shown in Fig. S1 (ESI †), the molecular conformations of both compounds show negligible changes with the increase of temperature. In contrast, all the distances of CH $\cdots\pi$ and CH \cdots N interactions are increased, indicating the decrease of intermolecular interactions in both crystals with increasing temperature. Note that **TPA-DPP** also shows a more compact packing than **TPA-DPQ** at 293 K, which may govern the fluorescence emission.

3.4 UV-vis absorption and emission spectra of **TPA-DPQ** and **TPA-DPP** in different solvents

Fig. 4a and b show the photographs of **TPA-DPQ** and **TPA-DPP** in several solvents with various polarities under 365 nm UV excitation. UV-vis absorption spectra of **TPA-DPQ** in *n*-hexane show two major absorption bands at 310 and 400 nm (Fig. 2c and Table 3), corresponding to the π - π^* transition and intramolecular charge transfer (ICT) transition, respectively. **TPA-DPP** also exhibits a similar absorption pattern with two bands at 350 and 425 nm (Fig. 2d and Table 3) in *n*-hexane.

Table 3 Spectral properties of **TPA-DPQ** and **TPA-DPP** in different solvents

Solvent	Δf (ϵ , n)	TPA-DPQ			TPA-DPP		
		λ_{abs} (nm)	λ_{em} (nm)	$\Delta\nu$ (cm^{-1})	λ_{abs} (nm)	λ_{em} (nm)	$\Delta\nu$ (cm^{-1})
<i>n</i> -Hexane	0.001	400	448	2678	425	465	2024
Toluene	0.013	404	483	4048	427	520	4188
THF	0.210	411	532	5534	438	585	5737
DCM	0.217	402	570	7732	426	628	7551
DMF	0.274	400	618	8819	423	723	9809

From the absorption edge, the E_g values of the two compounds are estimated to be 2.54 and 2.32 eV, which are lower than those obtained in the theoretically calculated values by *ca.* 0.6 eV, which can be attributed to the calculations that are employed under the gas-phase conditions. With the increase of solvent polarity from *n*-hexane to *N,N*-dimethylformamide, the absorption spectra of **TPA-DPQ** and **TPA-DPP** are slightly altered, indicating the insignificant effects of solvent polarity on the ground-state electron distribution.

As shown in Fig. 4e and Table 3, **TPA-DPQ** in hexane (nonpolar solvent) shows deep blue emission peaking at 448 nm with a small Stokes shift ($\Delta\nu$) of 2678 cm^{-1} , while the emission peak of **TPA-DPQ** undergoes a red-shift to 618 nm in *N,N*-dimethylformamide (polar solvent) with a large $\Delta\nu$ of 8819 cm^{-1} , whereas **TPA-DPP** shows a sky blue ($\lambda_{\text{em}} = 465$ nm, $\Delta\nu = 2024$ cm^{-1}) and deep red ($\lambda_{\text{em}} = 723$ nm, $\Delta\nu = 9809$ cm^{-1}) color in hexane and *N,N*-dimethylformamide, respectively. (Fig. 4f) These results indicate that the excited states of both compounds can be stabilized in polar solvents, implying typical ICT characteristics. The solvent-dependent Stokes shifts for **TPA-DPQ** and **TPA-DPP** are then analyzed from the Lippert-Mataga eqn (1):^{44,45}

$$\Delta\nu = \nu_a - \nu_f = (2\Delta\mu^2/hca^3)\Delta f(\epsilon, n) + A; \quad (1)$$

where $\Delta f(\epsilon, n)$ is calculated from eqn (2):

$$\Delta f(\epsilon, n) = [(\epsilon - 1)/(2\epsilon + 1)] - [(n^2 - 1)/(2n^2 + 1)]. \quad (2)$$

Here, $\Delta\mu$ is the difference between the excited- and ground-state dipole moments upon excitation, h is Planck's constant (6.6×10^{-34} J s $^{-1}$), c is the velocity of light in a vacuum (3.0×10^8 m s $^{-1}$), a is the Onsager cavity radius, and n and ϵ are the reflective index and the static dielectric constant of the solvents, respectively. As shown in Fig. 4g and Table 3, the slope values of **TPA-DPQ** and **TPA-DPP** are calculated to be 23398 and 28516 cm^{-1} , respectively. From the single crystal structures (Fig. 3), the a values of **TPA-DPQ** and **TPA-DPP** are both estimated to be 0.7157 nm. Accordingly, the $\Delta\mu$ values of

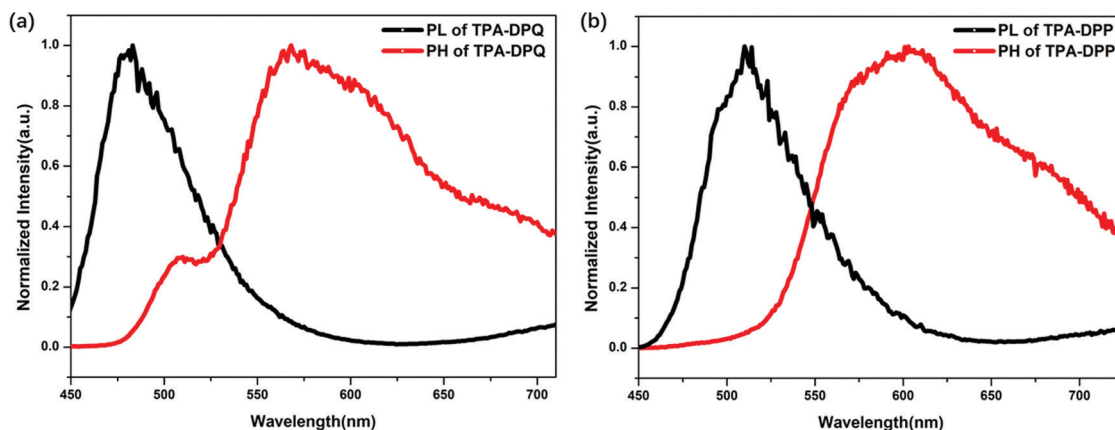


Fig. 5 (a) The time-resolved PL and PH spectra of **TPA-DPQ** in 2-MeTHF with 1 ms delay at 77 K; (b) the time-resolved PL and PH spectra of **TPA-DPP** in 2-MeTHF with 1 ms delay at 77 K.

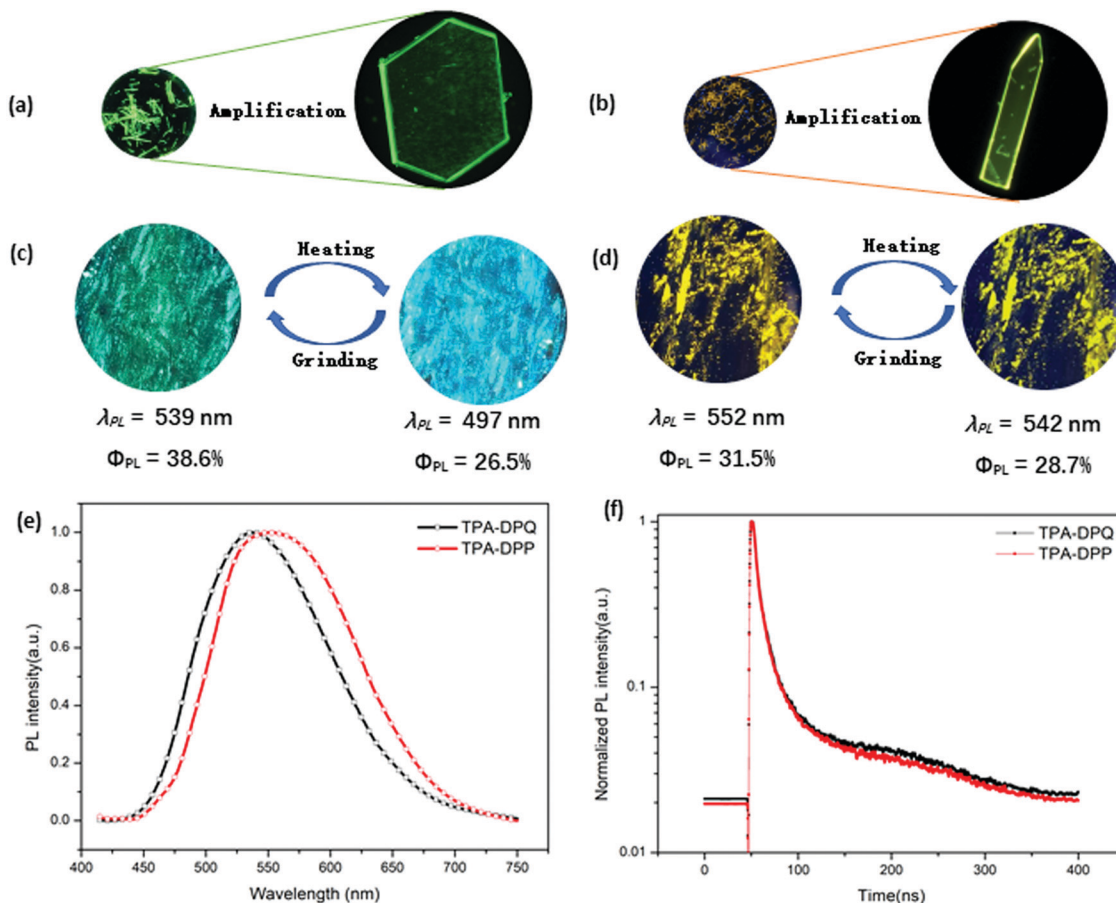


Fig. 6 (a) Fluorescence images of TPA-DPQ crystals; (b) fluorescence images of TPA-DPP crystals; (c) fluorescence images of TPA-DPQ solid response to grinding and heating under UV light (365 nm); (d) fluorescence images of TPA-DPQ solid response to grinding and heating under UV light (365 nm); (e) PL spectra of TPA-DPQ and TPA-DPP crystals; (f) PL decay curves of TPA-DPQ and TPA-DPP crystals.

TPA-DPQ and TPA-DPP are calculated to be 27.8 and 30.7 D, respectively. TPA-DPP has a larger $\Delta\mu$ than TPA-DPQ, suggesting more efficient ICT between the donor TPA and the acceptor DPP than the electronic communication between TPA and DPQ.

Transient PL decays of TPA-DPQ and TPA-DPP are investigated. In DCM, both compounds exhibit nanosecond-scaled decay properties with lifetimes of 8.12 and 5.12 ns for TPA-DPQ and TPA-DPP (Fig. 4h), respectively, indicating typical fluorescence emission.

To estimate the energy levels of TPA-DPQ and TPA-DPP, the time-resolved PL and phosphorescence (PH, with 1 ms delay) spectra are examined in 2-MeTHF at 77 K. As shown in Fig. 5a and b, TPA-DPQ and TPA-DPP exhibit finely structured PL spectra with peaks at 482 and 514 nm. The corresponding S_1 values are calculated to be 2.57 and 2.41 eV, respectively. From the PH spectra of TPA-DPQ and TPA-DPP with peaks at 571 and 603 nm, their T_1 values are obtained to be 2.17 and 2.06 eV. Thus, the ΔE_{ST} values of TPA-DPQ and TPA-DPP are estimated to be 0.40 and 0.35 eV, respectively, which agree well with the theoretically calculated values.

3.5 MCL of TPA-DPQ and TPA-DPP

As shown in Fig. 6a-e and Table 4, the single crystals of TPA-DPQ and TPA-DPP show broad fluorescence with PL peaks at

537 and 551 nm, respectively. Absolute Φ_{PL} values and transient PL decays of the two compounds are also measured (Table 4). Both crystals exhibit short-lived nanosecond-scaled lifetimes. The radiation rate constants of TPA-DPQ and TPA-DPP are estimated to be 5.22×10^7 and 5.56×10^7 s⁻¹. Compared with TPA-DPP, TPA-DPQ exhibits a higher Φ_{PL} , which may be attributed to the suppressed non-radiative transition associated with weaker intermolecular interactions in the crystals (Fig. 3).

As shown in Fig. 6c, similar to the single crystals of TPA-DPQ, the as-prepared solid also emits green fluorescence with a maximum at 539 nm and a Φ_{PL} of 0.386. When the solid is heated at 120 °C for 10 s, the emission color of the powder is

Table 4 PL characteristics of TPA-DPQ and TPA-DPP in the solid state

	TPA-DPQ			TPA-DPP		
	Crystal	Solid	Heated solid	Crystal	Solid	Heated solid
λ_{PL} (nm)	537	539	497	551	552	542
Φ_{PL}	0.361	0.386	0.265	0.337	0.315	0.287
τ (ns)	6.92	7.24	7.66	6.06	7.28	7.75
k_r (10^7 s ⁻¹)	5.22	5.33	3.46	5.56	4.33	3.70
k_{nr} (10^7 s ⁻¹)	8.80	8.48	9.60	10.94	9.41	9.20

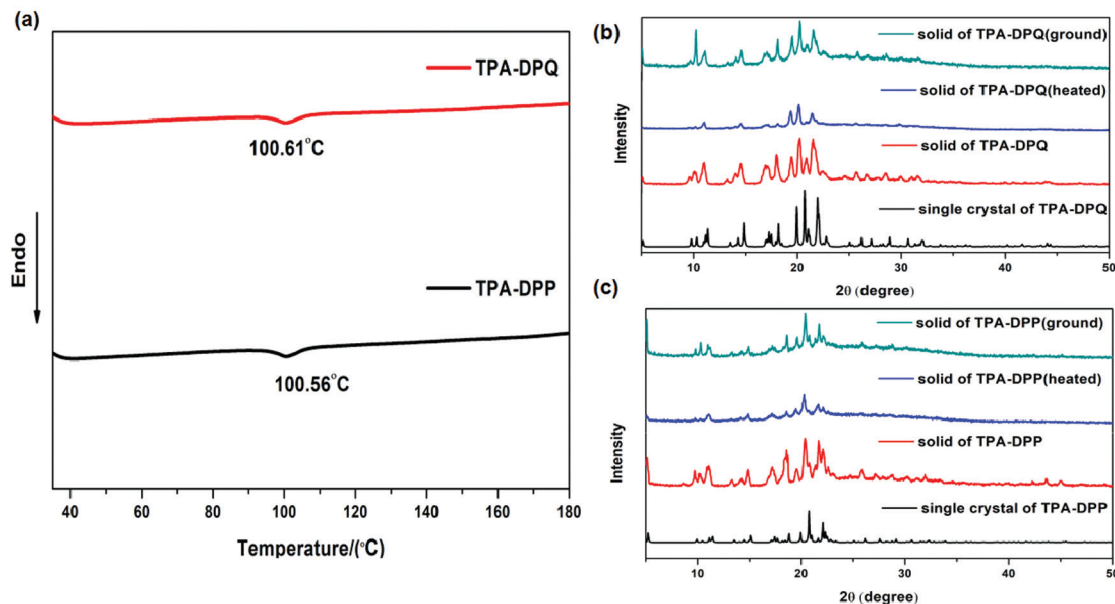


Fig. 7 (a) DSC curves of the as-prepared **TPA-DPQ** and **TPA-DPP** solids; (b) XRD spectra of **TPA-DPQ** in different states; (c) XRD spectra of **TPA-DPP** in different states.

switched to blue with a maximum at 497 nm and a Φ_{PL} of 0.265. Interestingly, the emission of the powder is transformed back to green after being ground. The reversible transformation in emission color in response to external stimuli indicates obvious MCL property of **TPA-DPQ**. Note that **TPA-DPQ** shows a large difference in emission color change ($\Delta\lambda_{\text{em}}$) of 42 nm upon external stimuli, which is comparable with other MCL emitters.¹⁵ In contrast, the solid of **TPA-DPP** also shows reversible emission color between yellow ($\Phi_{\text{PL}} = 0.315$, $\lambda_{\text{PL}} = 552$ nm) and yellowish green ($\Phi_{\text{PL}} = 0.287$, $\lambda_{\text{PL}} = 542$ nm) upon external stimuli, while the $\Delta\lambda_{\text{em}}$ is decreased to 10 nm. Obviously, **TPA-DPQ** and **TPA-DPP** exhibit different MCL features. During heat treatment, intermolecular interactions decrease as mentioned above, resulting in red-shifted PL emission.⁶ In this case, due to the more compact packing associated with stronger $\text{CH}\cdots\pi$ and $\text{CH}\cdots\text{N}$ intermolecular interactions, **TPA-DPP** is likely to be more stable upon heat treatment, inducing a small $\Delta\lambda_{\text{em}}$. In contrast, the large $\Delta\lambda_{\text{em}}$ of **TPA-DPQ** might be attributed to the loose packing associated with weaker $\text{CH}\cdots\pi$ and $\text{CH}\cdots\text{N}$ intermolecular interactions.

To gain insight on the origin of the MCL properties of **TPA-DPQ** and **TPA-DPP**, DSC experiments are performed. As can be seen from the DSC curves (Fig. 7a), during the heating process, the as-prepared solids of **TPA-DPQ** and **TPA-DPP** show similar endothermic peaks at 100.61 and 100.56 °C, respectively, indicating the phase transitions of both compounds. To further investigate the MCL behaviors of **TPA-DPQ** and **TPA-DPP**, PXRD measurements are carried out for respective samples. As expected, the diffraction curves of the as-prepared solids of **TPA-DPQ** and **TPA-DPP** exhibit sharp and strong diffraction peaks, which are similar to the simulated data of the single crystals of the corresponding compounds,

suggesting that the as-prepared solids have the same crystal systems as the corresponding single crystals for the two compounds. The results are in agreement with the similar emission properties of the as-prepared solids and the corresponding single crystals. In contrast, after being heated at 120 °C for 10 s, some strong and evident diffraction peaks of the as-prepared solids disappear, indicating the crystal phase transformations of **TPA-DPQ** and **TPA-DPP** during the heat treatment.³⁸ Upon grinding the heated solid, some strong and evident diffraction peaks appear again, which are similar to those of the corresponding as-prepared solid. The results coincide with the reversible PL color changes of the two compounds during the heating and grinding treatments. It is demonstrated that the phase transformations upon external stimuli should be responsible for the MCL behaviors of **TPA-DPQ** and **TPA-DPP**.

4. Conclusions

In conclusion, we synthesized a series of light-emitting analogues **TPA-DPQ** and **TPA-DPP**, which exhibit strong fluorescence emission in solutions and in solid states. Interestingly, **TPA-DPQ** and **TPA-DPP** show different MCL properties with $\Delta\lambda_{\text{em}}$ of 42 and 10 nm, respectively. Crystallographic analysis demonstrates that the significantly different MCL behaviors of the two compounds can be attributed to the subtle changes of $\text{CH}\cdots\pi$ and $\text{CH}\cdots\text{N}$ intermolecular interactions. This work will provide a guideline for further design of MCL emitters.

Conflicts of interest

There are no conflicts to declare.

Acknowledgements

This work was supported by the China Postdoctoral Science Foundation Funded Project (No. 2020M681464), the Qing Lan Project of Jiangsu Province, and the Natural Science Foundation of the Jiangsu Higher Education Institutions of China (No. 19KJB150006).

References

- 1 Y. Sagara and T. Kato, *Nat. Chem.*, 2009, **1**, 605.
- 2 G. Q. Zhang, J. W. Lu, M. Sabat and C. L. Fraser, *J. Am. Chem. Soc.*, 2010, **132**, 2160.
- 3 Z. Chi, X. Zhang, B. Xu, X. Zhou, C. Ma, Y. Zhang, S. Liu and J. Xu, *Chem. Soc. Rev.*, 2012, **41**, 3878.
- 4 Y. Sagara, S. Yamane, M. Mitani, C. Weder and T. Kato, *Adv. Mater.*, 2016, **28**, 1073.
- 5 Q. Qi, C. Li, X. Liu, S. Jiang, Z. Xu, R. Lee, M. Zhu, B. Xu and W. Tian, *J. Am. Chem. Soc.*, 2017, **139**, 16036.
- 6 K. Isayama, N. Aizawa, J. Y. Kim and T. Yasuda, *Angew. Chem., Int. Ed.*, 2018, **57**, 11982.
- 7 J. Yang, J. Qin, P. Geng, J. Wang, M. Fang and Z. Li, *Angew. Chem., Int. Ed.*, 2018, **57**, 16407.
- 8 B. Huang, D. Jiang, Y. Feng, W.-C. Chen, Y. Zhang, C. Cao, D. Shen, Y. Ji, C. Wang and C.-S. Lee, *J. Mater. Chem. C*, 2019, **7**, 9808.
- 9 Q. Li and Z. Li, *Adv. Sci.*, 2017, **4**, 1600484.
- 10 E. Ubba, Y. Tao, Z. Yang, J. Zhao, L. Wang and Z. Chi, *Chem. – Asian J.*, 2018, **13**, 3106.
- 11 X. L. Luo, J. N. Li, C. H. Li, L. P. Heng, Y. Q. Dong, Z. P. Liu, Z. S. Bo and B. Z. Tang, *Adv. Mater.*, 2011, **23**, 3261.
- 12 J. Q. Shi, N. Chang, C. H. Li, J. Mei, C. M. Deng, X. L. Luo, Z. P. Liu, Z. S. Bo, Y. Q. Dong and B. Z. Tang, *Chem. Commun.*, 2012, **48**, 10675.
- 13 T. Hu, B. C. Yao, X. J. Chen, W. Z. Li, Z. G. Song, A. J. Qin, J. Z. Sun and B. Z. Tang, *Chem. Commun.*, 2015, **51**, 8849.
- 14 B. Xu, J. He, Y. Mu, Q. Zhu, S. Wu, Y. Wang, Y. Zhang, C. Jin, C. Lo, Z. Chi, A. Lien, S. Liu and J. Xu, *Chem. Sci.*, 2015, **6**, 3236.
- 15 Z. Yang, Z. Chi, Z. Mao, Y. Zhang, S. Liu, J. Zhao, M. P. Aldred and Z. Chi, *Mater. Chem. Front.*, 2018, **2**, 861.
- 16 N. D. Nguyen, G. Zhang, J. Lu, A. E. Sherman and C. L. Fraser, *J. Mater. Chem.*, 2011, **21**, 8409.
- 17 Y. Gong, P. Zhang, Y. Gu, J. Wang, M. Han, C. Chen, X. Zhan, Z. Xie, B. Zou, Q. Peng, Z. Chi and Z. Li, *Adv. Opt. Mater.*, 2018, **6**, 1800198.
- 18 J. Yang, X. Gao, Z. Xie, Y. Gong, M. Fang, Q. Peng, Z. Chi and Z. Li, *Angew. Chem., Int. Ed.*, 2017, **56**, 15299.
- 19 Y. Dong, B. Xu, J. Zhang, X. Tan, L. Wang, J. Chen, H. Lv, S. Wen, B. Li, L. Ye, B. Zou and W. Tian, *Angew. Chem., Int. Ed.*, 2012, **51**, 10782.
- 20 Y. Gong, Y. Tan, J. Liu, P. Lu, C. Feng, W. Z. Yuan, Y. Lu, J. Z. Sun, G. He and Y. Zhang, *Chem. Commun.*, 2013, **49**, 4009.
- 21 Y. Gong, Y. Zhang, W. Z. Yuan, J. Z. Sun and Y. Zhang, *J. Phys. Chem. C*, 2014, **118**, 10998.
- 22 S. Xu, T. Liu, Y. Mu, Y. F. Wang, Z. Chi, C. C. Lo, S. Liu, Y. Zhang, A. Lien and J. Xu, *Angew. Chem., Int. Ed.*, 2015, **54**, 874.
- 23 B. Huang, Z. Li, H. Yang, D. Hu, W. Wu, Y. Feng, W. Jiang, B. Lin and Y. Sun, *J. Mater. Chem. C*, 2017, **5**, 12031.
- 24 J. Guo, X.-L. Li, H. Nie, W. Luo, S. Gan, S. Hu, R. Hu, A. Qin, Z. Zhao, S.-J. Su and B. Z. Tang, *Adv. Funct. Mater.*, 2017, **27**, 1606458.
- 25 M. Okazaki, Y. Takeda, P. Data, P. Pander, H. Higginbotham, A. P. Monkman and S. Minakata, *Chem. Sci.*, 2017, **8**, 2677.
- 26 E. Ubba, Y. Tao, Z. Yang, J. Zhao, L. Wang and Z. Chi, *Chem. – Asian J.*, 2018, **13**, 3106.
- 27 Y. Chen, S. Wang, X. Wu, Y. Xu, H. Li, Y. Liu, H. Tong and L. Wang, *J. Mater. Chem. C*, 2018, **6**, 12503.
- 28 X. Zeng, T. Zhou, J. Liu, K. Wu, S. Li, X. Xiao, Y. Zhang, S. Gong, G. Xie and C. Yang, *Adv. Opt. Mater.*, 2018, **6**, 1801071.
- 29 B. Huang, W.-C. Chen, Z. Li, J. Zhang, W. Zhao, Y. Feng, B. Z. Tang and C.-S. Lee, *Angew. Chem., Int. Ed.*, 2018, **57**, 12473.
- 30 W. Yang, Y. Yang, Y. Qiu, X. Cao, Z. Huang, S. Gong and C. Yang, *Mater. Chem. Front.*, 2020, **4**, 2047.
- 31 H. Zhang, Y. Wu, W. Zhang, E. Li, C. Shen, H. Jiang, H. Tian and W. Zhu, *Chem. Sci.*, 2018, **9**, 5919.
- 32 M. R. Reddy, S. H. Han, J. Y. Lee and S. Y. Seo, *Dyes Pigm.*, 2018, **153**, 132.
- 33 Y. Chen, Y. Ling, L. Ding, C. Xian and G. Zhou, *J. Mater. Chem. C*, 2016, **4**, 8496.
- 34 J. Sun, G. Zhang, X. Jia, P. Xue, J. Jia and R. Lu, *Acta Chim. Sin.*, 2016, **74**, 165.
- 35 J. Zhao, J. Sun, O. Simalou, H. Wang, J. Peng, L. Zhai, P. Xue and R. Lu, *Dyes Pigm.*, 2018, **151**, 296.
- 36 R. Pashazadeh, P. Pander, A. Lazauskas, F. B. Dias and J. V. Grazulevicius, *J. Phys. Chem. Lett.*, 2018, **9**, 1172.
- 37 Y. Zhan and H. Hu, *Dyes Pigm.*, 2019, **167**, 127.
- 38 R. Pashazadeh, G. Sych, S. Nasiri, K. Leitonas, A. Lazauskas, D. Volyniuk, P. J. Skabara and J. V. Grazulevicius, *Chem. Eng. J.*, 2020, **401**, 125962.
- 39 Y. Zhan and Y. Wang, *Dyes Pigm.*, 2020, **173**, 107971.
- 40 H. Wang, G. Chen, Y. Liu, L. Hu, X. Xu and S. Ji, *Dyes Pigm.*, 2009, **83**, 269.
- 41 CCDC 2065097 (TPA-DPQ at 150 K), 2075146 (TPA-DPQ at 296 K), 2065098 (TPA-DPP at 193 K) and 2080880 (TPA-DPP at 296 K)†.
- 42 *Gaussian 09 (Revision A.01)*, Gaussian, Inc., Wallingford, CT, 2009.
- 43 S. Y. Lee, T. Yasuda, Y. S. Yang, Q. Zhang and C. Adachi, *Angew. Chem., Int. Ed.*, 2014, **53**, 6402.
- 44 S. Sumalekshmy and K. R. Gopidas, *J. Phys. Chem. B*, 2004, **108**, 3705.
- 45 N. Mataga, Y. Kaifu and M. Koizumi, *Bull. Chem. Soc. Jpn.*, 1956, **29**, 465.